Ocean Engineering 292 (2024) 116571

Contents lists available at ScienceDirect

Ocean Engineering

journal homepage: www.elsevier.com/locate/oceaneng

Implications of wave–current interaction on the dynamic responses of a floating offshore wind turbine☆

Mujahid Elobeid [a,b,*], Ajit C. Pillai [a,c], Longbin Tao [a,b], David Ingram [a,d], Jan Erik Hanssen [e], Pedro Mayorga [e]

[a] EPSRC and NERC Industrial Centre for Doctoral Training in Offshore Renewable Energy (IDCORE), The University of Edinburgh, King's Buildings, Edinburgh EH9 3FB, UK
[b] Department of Naval Architecture, Ocean and Marine Engineering, University of Strathclyde, Glasgow G4 0LZ, UK
[c] Renewable Energy Group, Engineering Discipline, Faculty of Environment, Science, and Economy, University of Exeter, Penryn Campus, Penryn TR10 9FE, UK
[d] Institute for Energy Systems, School of Engineering, The University of Edinburgh, King's Buildings, Edinburgh EH9 3FB, UK
[e] EnerOcean S.L., Bulevar Louis Pasteur, n° 5, of.321, 29010 Málaga, Spain

ARTICLE INFO

Keywords:
Floating offshore wind turbines (FOWTs)
Wave–current interaction (WCI)
Nonlinear mooring dynamics
Combined wave and current
Dispersion relation
Semisubmersible
W2Power

ABSTRACT

This study investigates the implications of wave–current interaction on the dynamic responses of the W2Power semisubmersible platform for floating offshore wind turbines under operational and extreme conditions. Firstly, two analytical models based on Airy wave theory are developed to analyse the effects of current interaction with regular and irregular waves. Then, these models are integrated with the well-known engineering tool OrcaFlex for the coupled aero-hydro-servo-elastic analysis. The presence of current was found to significantly modify the wave profiles and influence the static equilibrium, mooring system, and motion dynamics of the FOWT.

The results reveal that the translational motion responses, such as surge and heave, are affected by wave–current interaction, with mean and maximum values decreasing under a following current and increasing under an opposing current. However, rotational motion responses are minimally affected. Wave–current interaction also notably affects maximum mooring tensions, with variations of up to ±22% depending on the current direction and mooring layout. Furthermore, reductions in maximum longitudinal acceleration are observed due to such interaction. Incorporating wave–current interaction in simulations enhances our understanding of FOWT dynamics and allows for more reliable estimations of system behaviour, emphasising the importance of ensuring safe operating conditions, particularly in sites with opposing currents.

1. Introduction

Offshore wind is widely regarded as a significant renewable energy source for decarbonising power production and decreasing greenhouse gas emissions. Thus, substantial efforts are being made to design wind turbines capable of capturing energy at sea. These turbines can be installed on bottom-fixed or floating foundations anchored to the seabed by mooring lines. When it comes to the shallow water (e.g. the North Sea, Chinese coastal waters, and the New England coast) of soft seabeds (i.e. made of sand, gravel or mud), the deployment of bottom-fixed foundations is the most cost-effective and optimal option. However, some regions (e.g. the Mediterranean Sea) lack favourable seabed conditions for bottom-fixed foundations. Moreover, 80% of offshore wind potential is in waters deeper than 60 m, thereby bottom-fixed foundations are problematic (WindEurope, 2018). Hence, floating offshore foundations are emerging as potential revolutionary solutions that offer broader wind resource exploitation and alleviate problems associated with bottom-fixed designs.

These floating offshore wind turbines (FOWTs) are subjected to various environmental loads, such as wind, waves, and currents (see Fig. 1). For their design and lifetime safety, the dynamic response in storm conditions, as well as the static stability and coupled dynamic response under operation conditions, are of paramount importance and, hence, have been an ongoing research focus. The hydrodynamic

☆ This work was funded by the EPSRC and NERC Industrial Centre for Doctoral Training in Offshore Renewable Energy (EP/S023933/1). The authors are also grateful to the National and Kapodistrian University of Athens for providing the hindcast data.

* Corresponding author at: EPSRC and NERC Industrial Centre for Doctoral Training in Offshore Renewable Energy (IDCORE), The University of Edinburgh, King's Buildings, Edinburgh EH9 3FB, UK.
E-mail address: m.elobeid@ed.ac.uk (M. Elobeid).
URL: https://www.idcore.ac.uk (M. Elobeid).

https://doi.org/10.1016/j.oceaneng.2023.116571
Received 5 June 2023; Received in revised form 25 November 2023; Accepted 11 December 2023
Available online 16 December 2023

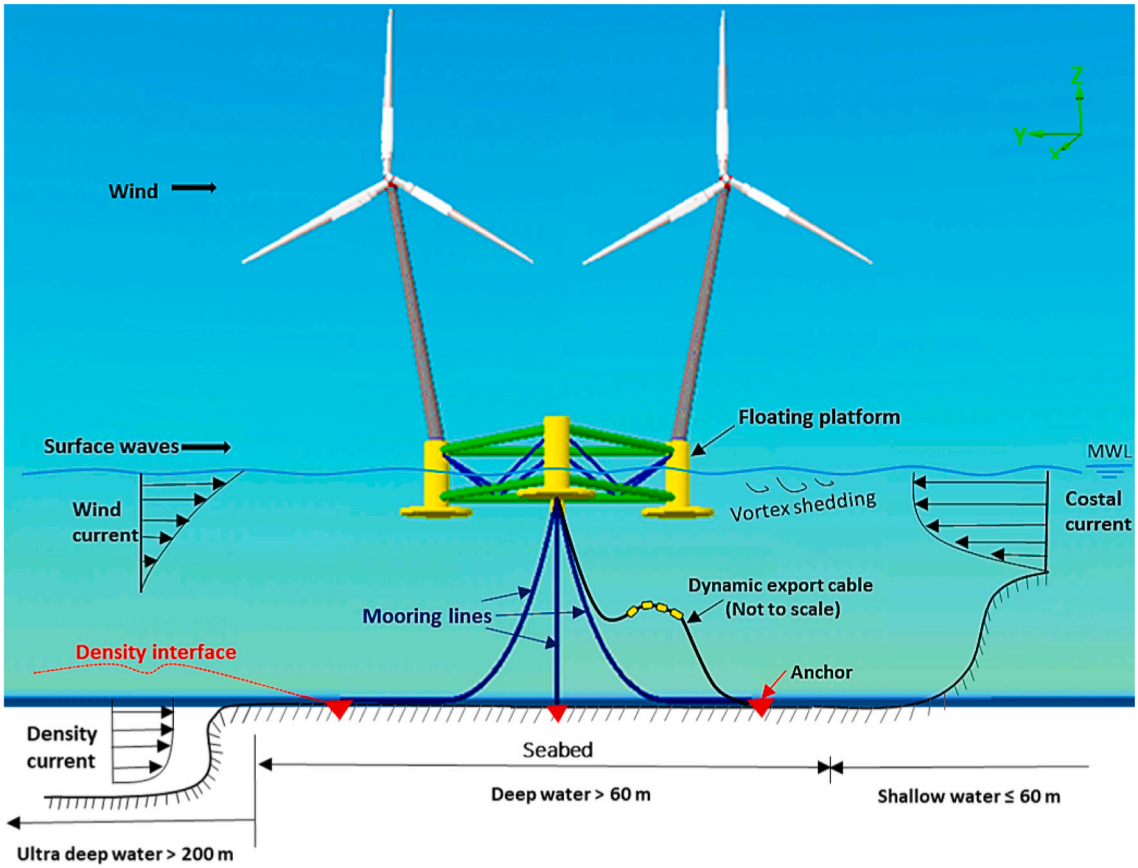

Fig. 1. Schematic showing the influence of wind-driven and near-shore currents on a floating platform moored in deep water.

loads due to the waves applied to the structure's large and slender elements are usually estimated using potential flow theory and Morison's formula, respectively (Morison et al., 1950). These hydrodynamic loads are composed of two components: (i) the drag force, which is proportional to the fluid particle velocity, and (ii) the inertia force, which is proportionate to fluid particle acceleration.

Sea currents are a potentially significant loading source for FOWTs that act as a constant lateral drag force on the platform, dynamic export cables, and mooring lines, and the DNV offshore standard recommends that they should be accounted for in mooring simulations (DNV, 2010). Nevertheless, previous investigations that utilised linearised or quasi-static cable models disregarded the current effects on mooring lines (Jonkman, 2007). These currents affect the operating point of the mooring system of FOWTs and result in the mooring lines' static, dynamic, and damping responses (Hall et al., 2014). Moreover, for the overall floating system, currents can cause floater vortex-induced motion (VIM), static offset, and augmented wave drift forces (Gonçalves et al., 2021). These currents may be triggered by winds, tides, or density changes, as illustrated in Fig. 1.

When waves propagate on a current, the interaction between the current and the waves results in frequency shifts (i.e. Doppler effect) and changes to the wave parameters (i.e. wavelength, amplitude, and spectral energy density); thus, a higher-velocity current substantially impacts the wave field through such interaction (Jonsson, 1990; Masson, 1996; Smith, 1997; Moreira and Peregrine, 2012). In shallow and intermediate water depths, the potential impacts of wave–current interaction (WCI) on fatigue loading for a single pile platform were identified physically i.e., using in-situ measurements (Peters and Boonstra, 1988) and emphasised numerically by methods of spectral fatigue analysis (Peeringa, 2014). Pillai et al. (2021) developed a framework to calculate current and current-modified wave parameters, showcasing the influence of WCI on fatigue loading of floating structures. Experiments further demonstrated the effects of WCI on both structural loads and VIM of these floating structures (Draycott et al., 2021).

In deep waters, where FOWTs are deployed and WCI coexist, this interaction impacts the dynamic responses of FOWTs during operational and extreme conditions. As a consequence, they might increase the platform's mean surge wave-drift force (Zhao et al., 1988) and lead to fatigue in the system's superstructures (e.g. mooring lines and towers) (Chen and Basu, 2018; Qu et al., 2020; Silva et al., 2021). However, the interaction of waves with an underlying current was found to have no significant impact on the performance of the system's pitch controller (Sarkar et al., 2020).

WCI has not yet been addressed extensively in the coupled analysis of FOWTs, and that is due to two key challenges that must be handled: a fully nonlinear mooring model capable of incorporating current and an appropriate WCI model. The recent development of nonlinear mooring models has addressed the first challenge; interested readers are referred to previous studies (Palm et al., 2016; Davidson and Ringwood, 2017; Pillai et al., 2018). However, the latter has not yet been overcome and is still an ongoing research topic. Moreover, most commercial engineering tools (e.g. FAST, Sima, OrcaFlex) employ the conventional superposition of waves and currents when defining the properties of waves, such as JONSWAP waves (Hasselmann et al., 1973). What is missing is the Doppler shift modification of the linear dispersion relationship that accounts for the effect of the current (Azcona et al., 2017). To overcome this limitation, new formulations and derivations for the total fluid particle velocity, the vector sum of the current velocity and wave-induced fluid particle velocity, are needed to incorporate Doppler shift appropriately. Subsequently, custom analytical models must be developed to account for the interaction between currents and waves (both regular and irregular) and then analyse the dynamic behaviours of FOWTs appropriately.

The well-known model for the interaction of regular waves and currents is based on the Airy wave theory, in which the current effects alter the wave frequency and dispersion relation (Thomas, 1981). For irregular waves, Huang et al. (1972) and Tung and Huang (1974) proposed analytical spectral models based on the solution of the regular wave model, and these models account for the impacts of the current on the wave spectrum (Huang et al., 1972; Tung and Huang, 1974). Hedges (1981) then extended these models to account for wave breaking driven by opposing or unfavourable currents (Hedges, 1981; Hedges et al., 1985). These models were verified and validated using numerical simulations and tests, respectively, and demonstrated sufficient accuracy for waves with small amplitudes (Thomas, 1981; Lai et al., 1989; Soares and De Pablo, 2006). They have been used in the design and structural response assessment of offshore structures, such as floating bridges and marine platforms (Ismail, 1984; Dai et al., 2022).

In offshore renewable energy applications, these models have been utilised to investigate the performance of marine tidal turbines and the fatigue loading of a bottom-fixed wind turbine (Barltrop et al., 2007; de Jesus Henriques et al., 2014; Peeringa, 2014). Recently, they were employed to assess the impact of WCI on the fatigue life and dynamic structural responses of a Spar FOWT. Quantitatively, the incorporation of wave–current interaction resulted in up to 10% differences in the dynamic responses of this FOWT and up to 15% increases in its cable fairlead tension (Chen and Basu, 2018, 2019). Additionally, Nguyen (2022) looked into the interaction effect of long-amplitude waves and currents on the same FOWT, finding that the FOWT drifted 15 m downstream in the presence of a favourable current. In contrast, when the current opposes the waves, the line fairlead tension can increase by up to 20% (Nguyen, 2022). Yet, the effects of WCI on single-point-mooring FOWTs have not been investigated. Yet, the effects of WCI on semisubmersible FOWTs that utilise single-point-mooring (SPM) systems have not been investigated.

Consequently, this paper looks into the effect of wave and current interaction on the mooring loads of an SPM system of a semisubmersible FOWT and explores how this interaction impacts the dynamic behaviour of the entire floating system under realistic environmental conditions. To achieve this, a nonlinear hydrodynamic model of the mooring system and analytical wave–current models are incorporated into a coupled analysis of the FOWT to account for the interaction. Following the introduction, the remainder of the paper is structured as follows: Section 2 presents the wave–current interaction models. Section 3 describes a coupled model for the numerical modelling of the W2Power floating wind turbine, focusing on the mooring system's hydrodynamic loading and nonlinear dynamics. The effects of wave–current interaction are then investigated numerically and discussed in Section 4. The results of the study are presented in Section 5 before the conclusions are discussed in Section 6.

2. Mathematical models of wave–current interaction

2.1. Governing equations

When wave and current fields coexist, the velocity potential can be divided into a steady current potential and an unsteady wave potential. Then, the water surface elevation surrounding the structure can be calculated by plugging both the unstable wave potential and the current velocity into the first-order dynamic surface boundary condition (Isaacson and Cheung, 1993). The following coordinate system (x, z), shown in Fig. 2, is defined to introduce the models for the wave–current flows. The origin, $O_{(0,0)}$, is assumed to be the mean water level (MWL), with the positive X-axis aligned horizontally in the direction of wave propagation, whereas the z-axis points vertically upward.

The continuity equation and momentum (Euler) equations governing the rotational flow of an inviscid and incompressible fluid are as follows:

$$\frac{\partial u}{\partial x} + \frac{\partial w}{\partial z} = 0 \tag{1}$$

$$\frac{\partial u}{\partial t} + u\frac{\partial u}{\partial x} + w\frac{\partial u}{\partial z} = -\frac{1}{\rho}\frac{\partial p}{\partial x} \tag{2}$$

$$\frac{\partial w}{\partial t} + u\frac{\partial w}{\partial x} + w\frac{\partial w}{\partial z} = -\frac{1}{\rho}\frac{\partial p}{\partial x} - g \tag{3}$$

where, u and w represent the horizontal and vertical components of fluid velocity, p, g, and ρ are the pressure, the gravitational acceleration and water density, respectively.

2.2. Regular wave–current mathematical model

For regular wave–current interaction, the model formulations given in Thomas (1981) and Silva et al. (2016) are roughly adopted, and the following flow assumptions are made:

- The flow field is irrotational,
- Waves are of small amplitudes and propagate on currents,
- No flow fluctuations exist perpendicular to the O_{xz} plane, and the waves undergo no refraction,
- The time and length scales of the current are relatively larger than the waves' period and wavelength.

Therefore, the resulting velocities (u_T and w_T) and pressure (p_T) fields are represented by the sum of the flow due to currents and waves:

$$u_T(x, z, t) = U(z) + u(z)\cos(\kappa x - \omega t) \tag{4}$$

$$w_T(x, z, t) = w(z)\sin(\kappa x - \omega t) \tag{5}$$

$$p_T(x, z, t) = -\rho g z + p\cos(\kappa x - \omega t) \tag{6}$$

where u, w, and p denote the magnitude of the perturbation caused by the wave, κ denotes the wave number in the direction of wave propagation (i.e. $\kappa = 2\pi/L$, L is the wavelength), and $U(z)$ is the current velocity profile as a function of water depth (h_w) in the absence of waves. ω is the wave's "apparent" angular frequency, and for an observer in a fixed reference system is the sum of the relative or intrinsic frequency in quiescent water (ω_r) and the Doppler frequencies (White, 1999) and can be written as:

$$\omega = \omega_r + \vec{\kappa} \cdot \vec{U} \tag{7}$$

in which, $\vec{\kappa}$ and $\vec{U}$ are, respectively, the vectors of the current velocity and wave number. In the linear Airy wave theory, the water surface elevation $\eta(x, t)$ is sinusoidal and can be expressed as:

$$\eta(x, t) = A\cos(\kappa x - \omega t) \tag{8}$$

in which A is the current-altered wave amplitude. Substituting the formulae of the resulting fields of velocities and pressure, Eq. (4)–(6), into the continuity, Eq. (1), and momentum equations, Eq. (2) and (3), gives:

$$\frac{\partial w}{\partial z} = \kappa u \tag{9}$$

$$p = \frac{\rho}{\kappa^2}\left[\frac{\partial w}{\partial z}(\omega - U(z)\kappa) + w(\kappa\frac{\partial U(z)}{\partial z})\right] \tag{10}$$

$$\frac{\partial p}{\partial z} = \rho w(\omega - U(z)\kappa) \tag{11}$$

After straightforward elimination of variables and some manipulation, Eq. (9)–(11) yield an alternate equation for vertical velocity, written as:

$$\frac{\partial^2 w}{\partial z^2} - \left[\kappa^2 - \frac{\kappa}{\omega - U(z)\kappa}\frac{\partial^2 U(z)}{\partial z^2}\right] w = 0 \tag{12}$$

Eq. (12) is known as the "inviscid Orr–Sommerfeld" or "Rayleigh" equation of classical hydrodynamic stability theory in the flow domain $-h_w < z < 0$, which must be solved in accordance with the rigid bottom boundary condition:

$$w_T = w(z) = 0 \quad \text{on } z = -h_w \tag{13}$$

and the mean free surface linearised boundary conditions:

$$w(z) = A(\omega - \kappa U(z)) \quad \text{on } z = 0 \tag{14}$$

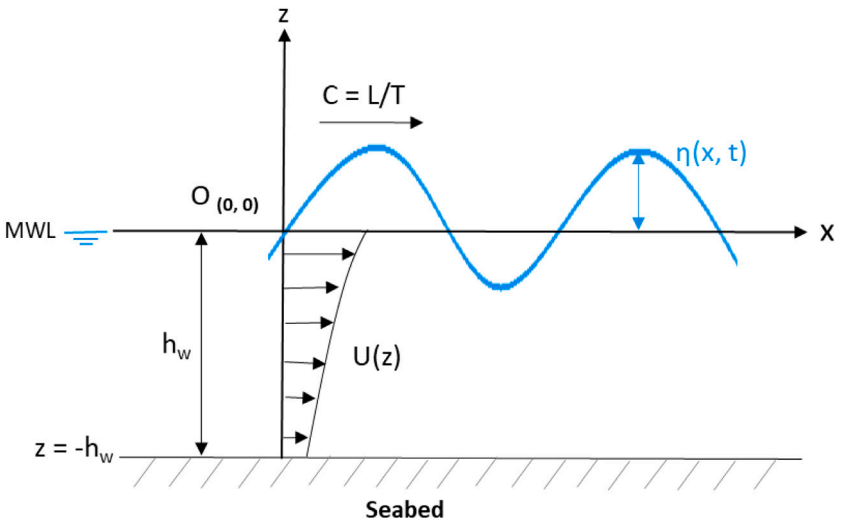

Fig. 2. Definition of the coordinate system for wave–current interaction of a finite depth.

$$p = \rho g A \quad \text{on } z = 0 \tag{15}$$

Substituting the boundary conditions on $z = 0$, Eq. (14) and (15), into the pressure field equation, Eq. (10), gives the current-affected dispersion relation.

$$(\omega - \kappa U(z))^2 \frac{\partial w}{\partial z} + \left[\kappa(\omega - \kappa U(z)) \frac{\partial U(z)}{\partial z} - g\kappa^2\right] w = 0 \tag{16}$$

If the parameters A, ω, and h_w, alongside $U(z)$, can be treated as known values in advance from experimental specifications or measurements, then the system of Eqs. (12)–(14) can be solved for the wavenumber κ and the vertical velocity $w(z)$. Accordingly, once these unknowns have been determined, the depth-varying component of the horizontal velocity $u(z)$ can be derived from the continuity equation, Eq. (1), as:

$$u(z) = \frac{1}{\kappa} \frac{\partial w}{\partial z} \tag{17}$$

However, the system is defined by the set of equations, Eq. (12), (13) and (16), cannot be solved analytically for general wavenumbers and frequencies unless the second derivative of the current velocity profile is equal to zero ($\frac{\partial^2 U(z)}{\partial z^2} = 0$), which corresponds to a depth-independent current or a current that changes linearly with depth. The Rayleigh equation, Eq. (12), can thus be rewritten as:

$$\frac{\partial^2 w}{\partial z^2} - \kappa^2 w = 0 \tag{18}$$

this Rayleigh equation, Eq. (18), depends on the vertical velocity $w(z)$ and the current velocity profile $U(z)$, and its solution for the wavelike horizontal velocity u(z) can be given by:

$$u(z) = A(\omega - U_0\kappa) \frac{\cosh[\kappa(z + h_w)]}{\sinh(\kappa h_w)}; \tag{19}$$

for $w(z)$ by:

$$w(z) = A(\omega - U_0\kappa) \frac{\sinh[\kappa(z + h_w)]}{\sinh(\kappa h_w)}; \tag{20}$$

and for $p(z)$ by:

$$p(z) = \rho A(\omega - \kappa U_0) \frac{1}{\kappa \sinh(\kappa h_w)} \times \left[(\omega - \kappa U(z)) \cosh[\kappa(z + h_w)] + \frac{dU(z)}{dz} \sinh[\kappa(z + h_w)]\right] \tag{21}$$

Substitution of Eqs. (19)–(21) in the resultant velocity and pressure fields, Eq. (4)–(6), yields:

$$u_T(x, z, t) = U(z) + A(\omega - U_0\kappa) \frac{\cosh[\kappa(z + h_w)]}{\sinh(\kappa h_w)} \cos(\kappa x - \omega t) \tag{22}$$

$$w_T(x, z, t) = A(\omega - \kappa U_0) \frac{\sinh[\kappa(z + h_w)]}{\sinh(\kappa h_w)} \sin(\kappa x - \omega t) \tag{23}$$

$$p_T(x, z, t) = -\rho g z + \frac{\rho A(\omega - \kappa U_0)}{\kappa \sinh(\kappa h_w)} \left([\omega - \kappa U(z)] \cosh(\kappa(z + h_w)) + \frac{\partial U(z)}{\partial z} \sinh(\kappa(z + h_w))\right) \cos(\kappa x - \omega t) \tag{24}$$

U_0 denotes the current velocity at $z = 0$. Substituting Eq. (20) into Eq. (16) gives the modified dispersion relation as:

$$(\omega - \kappa U_0)^2 = [g\kappa - (\omega - \kappa U_0) \frac{\partial U(z = 0)}{\partial z}] \tanh(\kappa h_w) \tag{25}$$

This equation is only valid for both uniform and linear shear current profiles (i.e. when $\frac{\partial^2 U(z)}{\partial z^2} = 0$). For the former, it can thus be simplified to the convenient form of the dispersion relation:

$$(\omega - \kappa U_0)^2 = g\kappa \tanh(\kappa h_w) \tag{26}$$

For a linear shear current profile that can be expressed by:

$$U(z) = U_0 + Bz \tag{27}$$

then the modified dispersion relation can be represented as:

$$(\omega - \kappa U_0)^2 = [g\kappa - (\omega - \kappa U_0)B] \tanh(\kappa h_w) \tag{28}$$

where B is the current slope, and Eq. (28) is true for $B = 0$ (i.e. uniform profile), and $B \neq 0$ (i.e. linear shear profile).

Based on the principle of 'wave-action' conservation (Bretherton and Garret, 1970), the modified wave amplitude of Eq. (8) in the presence of a current, (A), can be expressed as follows (Smith, 1997; Draycott et al., 2018):

$$A = A_a \left[\frac{C_{g,a}}{C_g} \cdot \frac{1}{1 + \frac{U \cos\alpha}{C_g}}\right]^{\frac{1}{2}}; \tag{29}$$

the subscript 'a' indicates a region with the absence of current, and α is the angle between the propagation directions of the wave and current, and C_g is the velocity of the wave group and is given as:

$$C_g = \frac{1}{2} C \left(1 + \frac{2\kappa h_w}{\sinh(2\kappa h_w)}\right); \tag{30}$$

where C is the wave apparent celerity, which is the sum of the wave celerity in the moving reference frame (C_a) and the current velocity

(U), and can be expressed by the wavelength (L) and the corresponding period (T) as:

$$C = C_a + U; \quad = \frac{L}{T} \tag{31}$$

2.3. Stochastic wave–current mathematical model

Under the wave and current assumptions described in Section 2.2, a stochastic wave–current interaction model can be established by coupling the spectral representation of irregular waves with the equations of the regular wave–current model (Huang et al., 1972) Consequently, the spectral density of surface waves in the presence of the current, $S(\omega, U)$, is given by:

$$S(\omega, U) = \frac{4S(\omega)}{\left[1 + \frac{4U\omega}{g}\right]^{1/2}\left[1 + \left(1 + \frac{4U\omega}{g}\right)^{1/2}\right]^2} \tag{32}$$

in which $S(\omega)$ spectral density of waves without the influence of current; U, ω, and g are the current speed, frequency, and gravitational acceleration, respectively. In this paper, the JONSWAP (Joint North Sea Wave Project) spectrum was selected to generate the irregular waves (Hasselmann et al., 1973), whose expression is:

$$S(\omega) = \frac{\alpha\, g^2}{\omega^5}\exp\left[-\frac{4}{5}\left[\frac{\omega_p}{\omega}\right]^4\right]\gamma^{\alpha} \tag{33}$$

where ω_p is the peak frequency, γ is the peak enhancement factor, and parameters α and σ are

$$\alpha = \exp\left[\left[-\frac{(\omega-\omega_p)^2}{2\omega_p^2\sigma^2}\right]\right], \quad \sigma = \begin{cases} 0.07 & \text{if } \omega < \omega_p \\ 0.09 & \text{if } \omega \geq \omega_p \end{cases}, \text{ respectively.}$$

From Eq. (32), waves tend to shorten and become steeper when they encounter an opposing current (i.e. when the current speed is negative), and vice versa for waves travelling with a following current. Thus, it is worth mentioning that when the current speed is negative, there is a cut-off frequency that can be determined using the following formula:

$$1 + \frac{4U\omega}{g} \geq 0 \tag{34}$$

Before this critical frequency ($\omega = -\frac{g}{4U}$), surface waves with frequencies close to it become extremely steep, and theoretically, beyond this frequency, no waves can exist. In reality, wave breaking will occur at the current threshold, and since the wave amplitude at this critical speed would be infinite; thus the waves break a long time before they reach this limit. However, breaking still impacts wave components that propagate onto the current, so there is a limit to how big waves can develop over a certain frequency range (Phillips, 1977). In order to address this issue, Hedges (1981) derived the following "equilibrium range limit" for deep water (Hedges, 1981; Hedges et al., 1985):

$$S_{ER}(\omega, U) = \frac{A^* g^2}{(\omega - \kappa U)^5}\frac{1}{1 + \frac{2U(\omega - \kappa U)}{g}} \tag{35}$$

in which "ER" denotes the equilibrium range, and A^* is a numerical (Phillips-like) constant for the waves generated on currents, its values provided by Phillips in the range $0.008 - 0.015$ (Phillips, 1977).

Given that the equilibrium range of the spectrum is associated with deep water, the preceding equation, Eq. (35), can be used to predict spectral densities for the current region whenever $S_{\mathrm{ER}}(\omega, U)$ is smaller than $S(\omega, U)$. Following that, alterations in the spectra corresponding to flow velocity and acceleration driven by the subsurface current can be estimated (Hedges et al., 1985; Soares and De Pablo, 2006; Peeringa, 2014). By employing these spectral representations, the sinusoidal water surface elevation $\eta(x, t)$ for ith wave components can be written as:

$$\eta(x, t) = \sum_{i=1}^{N} A_i \cos(\kappa_i x - \omega_i t + \phi_i) \tag{36}$$

in which ϕ is the random phase angle spread evenly between 0 and 2π, and N refers to the total number of wave components. In this stochastic model, the amplitude of the ith wave component with frequency interval $\Delta\omega$ is given by:

$$A_i = \left[2S(\omega_i, U)\Delta\omega\right]^{1/2} \tag{37}$$

The corresponding formulae for the resultant horizontal and vertical velocities and pressure fields are:

$$u_T(x, z, t) = U(z) + \sum_{i=1}^{N} A_i(\omega_i - \kappa_i U)\frac{\cosh[\kappa_i(z + h_w)]}{\sinh(\kappa_i h_w)}\cos(\kappa_i x - \omega_i t + \phi_i), \tag{38}$$

$$w_T(x, z, t) = \sum_{i=1}^{N} A_i(\omega_i - \kappa_i U)\frac{\sinh[\kappa_i(z + h_w)]}{\sinh(\kappa_i h_w)}\sin(\kappa_i x - \omega_i t + \phi_i), \tag{39}$$

$$p_T(x, z, t) = -\rho g z + \sum_{i=1}^{N}\frac{\rho A_i(\omega_i - \kappa_i U)^2\cosh[\kappa_i(z + h_w)]}{\kappa_i \sinh(\kappa_i h_w)} \times \cos(\kappa_i x - \omega_i t + \phi_i), \tag{40}$$

respectively. Differentiating the velocity fields equations, Eq. (38) and (39), with regard to time yields the corresponding resultant accelerations (i.e. the horizontal and vertical) as:

$$\dot{u}_T(x, z, t) = \sum_{i=1}^{N} A_i\omega_i(\omega_i - \kappa_i U)\frac{\cosh[\kappa_i(z + h_w)]}{\sinh(\kappa_i h_w)}\sin(\kappa_i x - \omega_i t + \phi_i), \tag{41}$$

$$\dot{w}_T(x, z, t) = \sum_{i=1}^{N} A_i\omega_i(\omega_i - \kappa_i U)\frac{\sinh[\kappa_i(z + h_w)]}{\sinh(\kappa_i h_w)}\cos(\kappa_i x - \omega_i t + \phi_i), \tag{42}$$

in which the wavenumber k_i will be obtained from the modified dispersion relation, Eq. (26), for each wave component. Although this model is stochastic, it cannot capture the nonlinear effects of wave and wave–current interaction because it relies on the linear wave theory. However, some nonlinear effects (e.g. fluid velocity and acceleration) can be captured by employing kinematic stretching techniques (e.g. vertical, extrapolation, and Wheeler) (Faltinsen, 1993; Nestegård et al., 2019; OrcaFlex, 2023).

3. W2Power floating offshore wind turbine model

3.1. Platform model description

In order to investigate the effects of wave–current interaction on the dynamic responses of FOWTs, this paper employs an innovative floating wind turbine model called W2Power as a case study. This model was developed by EnearOcean S.L. (2007), Spain, in 2015 and does not represent the current design of the platform (Hanssen et al., 2015). It is a triangular semisubmersible structure that houses a pair of wind turbines mounted on out-leaning towers. The platform is moored to the seabed via a single-point mooring system, whose lines are attached to the bottom of the front column (B). The main particulars of the platform are given in Table 1. The towers are conical tubular steel structures that are cantilevered at 15° on the top of the floater's stern columns (A and C) (Elobeid et al., 2022), with tower data adopted from the OC3-Hywind spar FOWT (Jonkman, 2010).

3.2. Mooring system characteristics

The configuration of the single-point mooring system is a typical catenary that comprises three lines placed symmetrically along the platform's Z-axis and spread by 120°, and these individual lines are made of stud-less chains. The W2Power is designed for water depths of 200 m, whilst this study focuses on a prospective deployment site of 80 m water depth. The scaled mooring system proposed by Elobeid et al. (2022) has been up-scaled, optimised and employed in the current study; its properties are given in Table 2.

Table 1
Main parameters of the W2Power platform.

Parameter	Value (unit)	Parameter	Value (unit)
Draft	15 m	Braces diameter	1.32 m
Water depth	80 m	Pontoons diameters	3 m
Column D height	25 m	Heave plates height	1.5 m
Column D diameter	5 m	Heave plates diameter	27 m
Corner columns height	25 m	Towers bases separation	90 m
Corner columns diameter	9 m	Towers' out-leaning angle	15°

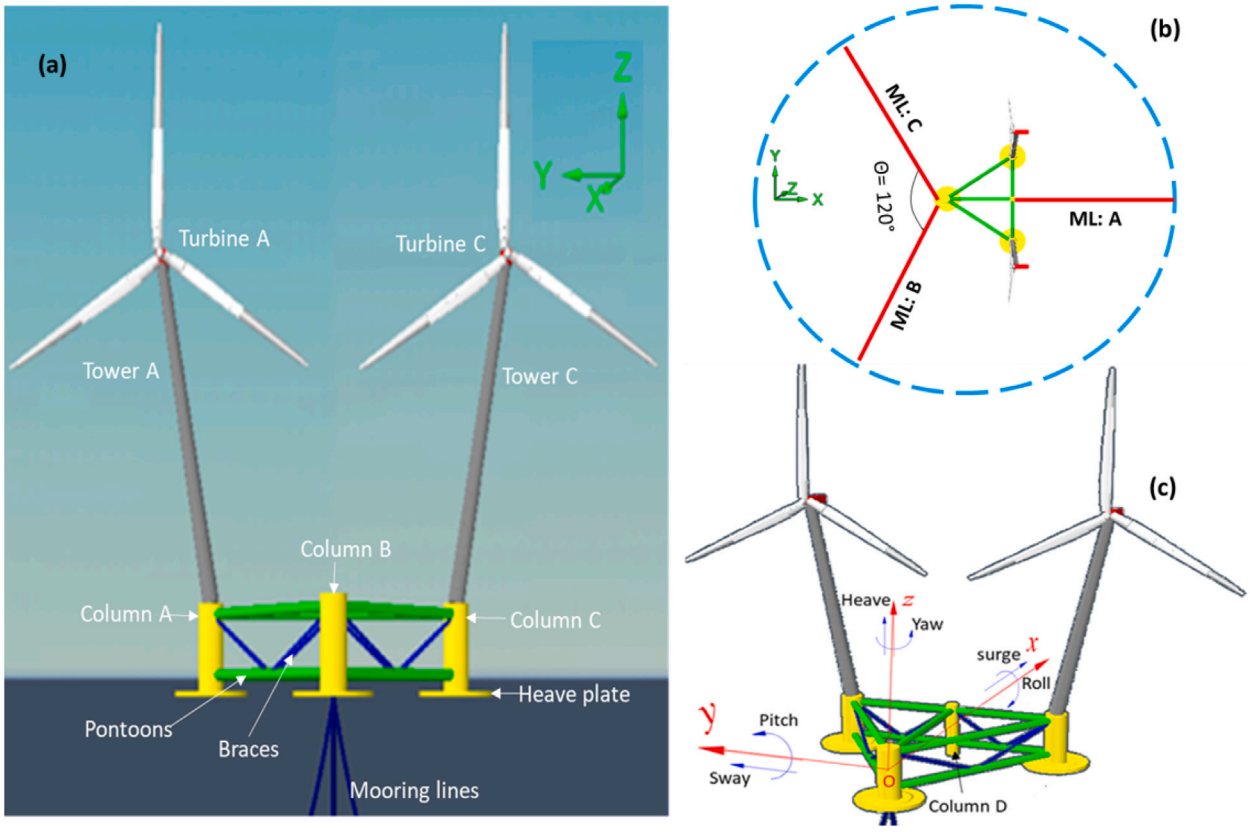

Fig. 3. Description of the W2Power FOWT: (a) the system's main particulars; (b) the mooring system configuration; (c) the 6 degrees-of-freedom of the system.

Table 2
Characteristics of the mooring system.

Parameter	Value (unit)	Parameter	Value (unit)
Fairlead depth	15 m	Line length	398.3 m
Number of lines	3	Axial stiffness	252.5E03 kN
Anchor depth, radius	80, 382.24 m	Line dry, wet weight	537, 466.4 kN/m
Line type (grade)	Chains (R4–Studless)	Fairlead pretension	1153 kN
Nominal chain diameter	157 mm	Minimum breaking load (MBL)	21235 kN

3.3. Floater-towers-nacelles-rotors model

The platform is engineered to accommodate two 6 MW wind turbines (WTs). Due to a lack of data on this WT, it is, therefore, analysed with a pair of the well-documented and publicly accessible NREL-5MW WT (Jonkman et al., 2009). The towers are conical tubular steel structures of a height of 77.6 m and base (platform top) and top diameters of 6.5 m and 3.87 m, respectively. They are cantilevered at an outward 15°atop the floater's stern columns (A and C). Towers' data are adopted from the OC3-Hywind spar FOWT (Shin, 2011), see Table 3.

The converging equation is established to calculate the displacement, velocity, and acceleration of the FOWT, as well as the mooring dynamics. It considers the effects of wind, wave, cable forces, and wave–current interaction, and is written to be solved for the 6 degrees-of-freedom (DoF) motions as follows:

$$(\mathbf{M}+\mathbf{A}_{\infty})\ddot{x}(t)+\int_0^t \mathbf{K}(t-\tau)\dot{x}(\tau)d\tau+\mathbf{B}\dot{x}(t)+\mathbf{C}x(t)=F_m(t)+F_h(t)+F_a(t) \quad (43)$$

this equation is known as Cummins equation, in which, $\mathbf{M}$ is the mass matrix of the entire FOWT including ballast, $\mathbf{A}_{\infty}$ is the added mass matrix at infinite frequency, and $\mathbf{K}(t)$ is the retardation function matrix (impulse response), which was calculated by the Cummins model (Cummins et al., 1962). The convolution integral handles the 'memory' effect of past motions (Rognebakke, 2002), whose τ is a 'time' variable ranging from 0 to t. $\mathbf{B}$ is the nonlinear damping matrix, and $\mathbf{C}$ is the stiffness matrix that comprises both the hydrostatic stiffness provided by buoyancy and the mooring stiffness, $\mathbf{C} = (\mathbf{C_h} + \mathbf{C_m})$. The displacement, velocity, and acceleration vectors of the body are, respectively, denoted by x, $\dot{x}$, and $\ddot{x}$. On the right side, F_m is the mooring

Table 3
Specifications of the NREL 5MW baseline wind turbine.

Parameter	Value (unit)	Parameter	Value (unit)
Rated power	5 MW	Rotor configuration	Upwind
Number of blades	3	Hub, rotor diameter	3, 126 m
Cut-in, rated rotor speed	6.9, 12.1 RPM	Drivetrain, control	Geared, pitch regulated
Cut-in, rated, cut-out wind speed	3, 11.4, 25 m/s	Rotor, nacelle, tower mass	110, 240, 249.7 tonne

fairlead tensions, F_h is the hydrodynamic loads (first- and second-order wave forces, and current drag force), and F_a is the aerodynamic loads on the two rotors.

4. Model setup for the implications of wave–current interaction

4.1. Platform-mooring modelling

The numerical modelling tools used are SolidWorks, DNV's Sesam-GeniE, and Orcina Ltd's OrcaWave and OrcaFlex (Solidworks, 2021; GeinE, 2020; OrcaWave, 2023; OrcaFlex, 2023). The floater's geometry was developed using SolidWorks, and its mass and inertia matrices were obtained. The hull's panel model (i.e. heave plates and columns) was meshed using GeniE, and a finite element file was subsequently generated. OrcaWave was then used to perform the diffraction analysis for the ballasted floater in the absence of the mooring system and superstructures (e.g. turbines, towers, nacelles). This yielded the floater's RAOs (response amplitude operator) and other hydrodynamic parameters such as the hydrostatic stiffness coefficients, the frequency-dependent hydrodynamic added mass and radiation damping, the first-and second-order wave forces, and difference-frequency quadratic transfer functions (QTFs). The OrcaWave-generated model was loaded as a vessel object into OrcaFlex to model the floater as a rigid body, whose motion is defined by three translations displacements (surge, sway, and heave) and three rotational displacements (roll, pitch, and yaw) at the body origin $(0, 0, 0)$ (see Fig. 3).

Then, three mooring lines were added between the platform's fairleads and the seafloor. Based on the properties listed in Table 2, the mooring cables were simulated using OrcaFlex's finite-element-method (FEM) model. Each line was discretised into segments, which were then modelled by straight massless model segments with a node at each end (Van den Boom, 1985). The model segments only capture the line's axial and torsional properties, whereas the other properties, like mass, weight, and buoyancy, were all lumped into the nodes (OrcaFlex, 2023). The seabed was assumed to be horizontal and on a rigid plane.

To account for the contribution of current-induced drag loads on viscous damping and mean platform offsets, the analysis considered drag loads on the submerged superstructures (mooring lines, heave plates, columns, pontoons, and braces). Thereby, an extended form of Morison's formula was employed to calculate the hydrodynamic loads on the mooring lines and platform (Morison et al., 1950; OrcaFlex, 2023), whose can be expressed as follows:

$$f = \overbrace{(C_m \Delta a_f - C_a \Delta a_b)}^{\text{Inertia}} + \overbrace{\left(\frac{1}{2}\rho C_d A |v_f| v_f\right)}^{\text{Drag}} \tag{44}$$

in which, f is the fluid force per unit length exerted on the body. C_m and C_a are, respectively, the inertia and added mass coefficients for the body, and the value of C_m was taken to be $1+C_a$. Δ denotes the mass of the fluid displaced by the body, and a_f is the fluid acceleration relative to the earth. ρ represents the density of water, C_d is the drag coefficient for the body, A is the drag area, and v_f is the fluid velocity relative to the earth.

4.2. Superstructures modelling

The superstructures (e.g. towers, heavy topsides) are modelled explicitly to include the rotors' rotation and flexing of the towers and blades in the OrcaFlex model. The towers are modelled as profiled cylinders via line objects that utilise homogeneous pipe attributes, which enable the modelling of variable outer and inner diameter profiles and their corresponding physical properties (e.g. mass and inertia). The rotors are then connected to the towers via nacelles that are modelled as lumped 6D buoys with their respective properties, and to increase blade-to-tower clearances, the rotors and nacelles are tilted by 5° (Jonkman et al., 2009). The blade structural model closely resembles a line model, with segmented blades and nodes at the ends of each segment. The blade discretisation and segment lengths were meticulously adjusted to be consistent with the overall length of the NREL-5MW turbine (Jonkman et al., 2009). At each node, the mass and inertia properties are appropriately grouped. Blade element momentum (BEM) theory is utilised to capture aerodynamic loads (Froude, 1920).

4.3. Modelling of wave–current interaction

Wave–current interaction is modelled in the Python programme to solve the linear dispersion relation, Eq. (26), and obtain the current-included wavenumber. It is not possible to solve Eq. (26) analytically; therefore, it is solved using the physical approximations by Fenton and McKee (1990). The presence of current slightly modifies the solution method; therefore, the well-known Newton–Raphson's method is used to refine the approximation. It is tailored to attain arbitrary customisable accuracy (Ben-Israel, 1966). Subsequently, these custom analytical models that account for the interaction between currents and waves (regular and irregular) are compiled as dynamic link libraries (DLLs) utilising the OrcaFlex Python API (i.e. Application Programming Interface), OrcFxAPI. The developed model incorporates two key aspects: the current effect on the mooring lines and the incorporation of WCI in hydrodynamic loading estimation on the FOWT. The coupled analysis model setup is shown in Fig. 4.

4.4. Environmental loads and simulation setup

This study investigates the performance of the W2Power platform at a reference site, Canari-I, off the coast of Gran Canaria in the Atlantic Ocean, whose environmental contours are constructed with a 50-year return period based on long-term hindcast data (wind, wave and current) (NKUA-AM&WFG, 2021). Different sea conditions are subsequently defined to represent both the "survival" and "operational" conditions. In extreme sea states, the turbines' rotors are parked. When the rotor is parked, the turbine blades are feathered to minimise the aerodynamic loads. This allows us to focus on the effects of WCI on the dynamic responses of the platform and mooring lines under such loading conditions. Whilst the aerodynamic loads and wind drag forces act on the wind turbine systems are included in the operational conditions. The rated wind speed (U_w) at the top of the towers is assumed to be 11.4 m/s, corresponding to the mean wind speed at 100 m hub height at the Canari-I site, and it is assumed to be in the same direction as the axes of the rotor and is modelled using the NPD (Norwegian Petroleum Directorate) spectrum with full field turbulent winds (Jonkman and Kilcher, 2012).

Different sea states are picked from the environmental contour, whose regular wave trains are defined by linear Airy types of height (H) and period (T). While the irregular ones are represented by the JONSWAP spectrum using a peak factor (γ), significant heights (H_s), and peak period (T_p). The Canari-I site has maximal and average

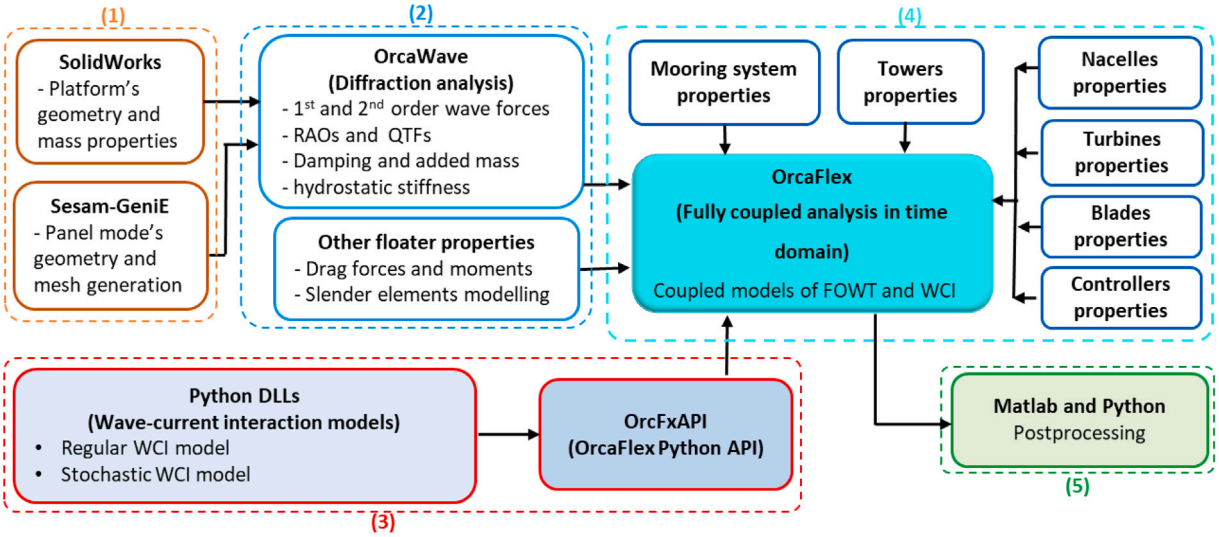

Fig. 4. Schematic flow chart of the coupled model setup and numerical modelling analysis.

Table 4
Load case parameters for coupled-analysis simulations of wave–current interaction.

LC No.	Wave model	H/H_s (m)	T/T_p (s)	γ	U_c (m/s)	Direction	U_w (m/s)
			Extreme sea states				
1	Regular	4.63	16	–	0.8	Following	0
2	Regular	4.63	16	–	0.8	Opposing	0
3	Regular	3.85	8	–	0.8	Following	0
4	Regular	3.85	8	–	0.8	Opposing	0
5	Irregular	4.63	16.4	3.3	0.8	Following	0
6	Irregular	4.63	16.4	3.3	0.8	Opposing	0
7	Irregular	3.85	9	3.3	0.8	Following	0
8	Irregular	3.85	9	3.3	0.8	Opposing	0
			Operational sea states				
9	Regular	1.4	7.4	–	0.3	Following	11.4
10	Regular	1.4	7.4	–	0.3	Opposing	11.4
11	Irregular	1.4	7.4	2	0.3	Following	11.4
12	Irregular	1.4	7.4	2	0.3	Opposing	11.4

current speeds (U_c) of 0.8 m/s and 0.3 m/s, respectively, whose profiles are characterised within OrcaFlex environment data.

In the simulations, the direction of the waves is fixed at 180°, and the current hits the platform from two directions, 180° and 0°, creating two current scenarios when interacting with waves, following and opposing, respectively. To assess the effect of current and the inclusion of wave–current interaction on the dynamic responses of the FOWT, the simulated scenarios are: (i) currents only; (ii) waves only; (iii) straightforward superposition of wave–current effects without considering any interaction; (iv) and incorporation of the wave–current interaction effects. Accordingly, the environmental conditions and identification numbers for all the load cases (LCs) considered are presented in Table 4.

5. Results and discussion

5.1. Current effects on wave fields

Wave–current interaction models established in Section 2 are used to examine the influence of current on regular and irregular waves. Two current velocities are considered: 0.3 and 0.8 m/s. For regular waves and utilising Eq. (8) and (29), current alters both the mean value and the amplitude of the wave free-surface elevation (η), whether the current is following or opposing, as shown in the left panel of Fig. 5. For clarity, a following current refers to a flow with a velocity in the same direction of wave propagation. In contrast, an opposing current propagates in the opposite direction as the waves, resulting in a negative velocity. Furthermore, frequency shifts were observed, as evident at the peaks of both the crests and troughs of the wave.

Eq. (32) and (35) are executed to generate the energy spectrum for stochastic waves with a JONSWAP spectrum of $\gamma = 1$, which reduces to the Pierson–Moskowitz (PM) spectrum (Pierson, Jr. and Moskowitz, 1964). In turn, the spectra are obtained for four different current velocities and shown on the right side of Fig. 5. The presence of current significantly modifies the peak value of the wave spectra. For opposing currents of speeds of −0.3 and −0.8 m/s, the peak spectral amplitude increases by 5% and 14.2%, respectively, while it decreases by 5% and 11.2% when the currents are following. The peak frequency is also shifted, as observed in the inset plots. Increasing the absolute value of the current speed results in a more significant alteration of the peak value and changes the shape of the wave spectrum. Furthermore, for opposite currents, the high-frequency tails of the spectra are adjusted using Eq. (35) with a Phillips's constant, A^*, of 0.015. Accordingly, the wave spectra are truncated beyond the cutoff frequency, and the cutoff frequency (i.e. $\text{cutoff} = 0.244$ Hz, 1.532 rad/s) is chosen to be four times the peak spectral frequency (i.e. $\text{peak} = 0.061$ Hz, 0.383 rad/s) (Jonkman, 2007). The results in Fig. 5 shed light on the fundamental physics of wave–current interaction in extreme and operational conditions at the reference site, Gran Canaria. The following subsections demonstrate the implications of these findings on the dynamic responses of the W2Power FOWT.

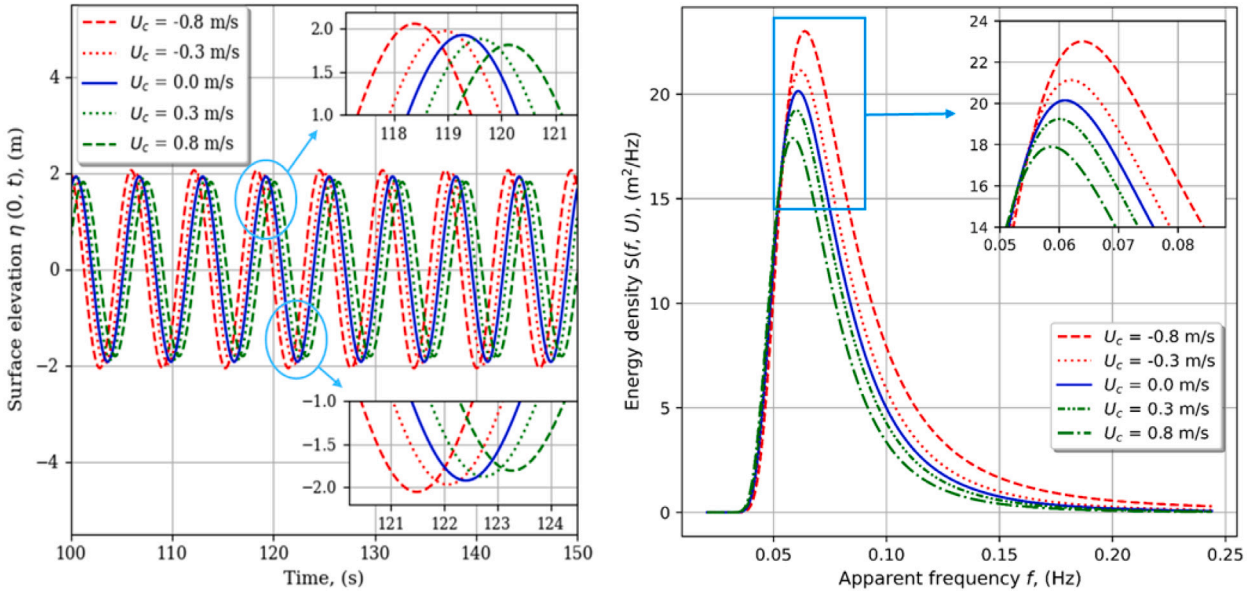

Fig. 5. Current effect on (left) the free surface elevation, $\eta(0,t)$, for a regular wave of H = 3.85 m and T = 6.2 s; and (right) the reduced JONSWAP spectrum of H_s = 4.63 m and T_p = 16.4 s.

5.2. Effect of wave–current interaction on motion dynamics

The simulation results for the FOWT system's motion responses under an operational load case (LC11) of an irregular wave with uniform current are shown in Fig. 6. The presence of the current induces offsets in the FOWT's structural responses and alters the system's equilibrium position; thereby, the current influences both the static and dynamic responses. To account for the current effect in simulating WCI load cases in OrcaFlex, the platform was first subjected to a pure current until it reached its static position. This new static position was then implemented in OrcaFlex, and the floater object's DoFs were deliberately deselected; by doing so, the current-modified wave file's effect on the platform's static analysis was incorporated. The simulations were run for 3800 s, with 200 s allotted for wave build-up and transient effect elimination. Thus, each load case analysis is an hour (3600 s) coupled simulation, which is enough for identifying the characteristics of the system dynamics according to the standards (DNV, 2019).

Fig. 6 illustrates the effect of wave–current interaction on the translational and rotational DoFs of the platform. Note that, herein, the mean values have been omitted to focus on the dynamic behaviour of the motion responses. Surge and heave DoFs were the most affected, while the pitch was moderately impacted, and the rest were less influenced. Despite wind damping the effect of WCI, there were slight changes in the mean values of surge, heave and pitch due to this interaction with a current speed of 0.3 m/s. Hypothetically, the interaction's effect should be more pronounced in the absence of wind, which is demonstrated in Fig. 7 for an extreme case of a current speed of 0.8 m/s. As can be seen, the mean values of the surge and heave decrease in the presence of the following current and increase with the opposing current due to the current drag force. Moreover, the relative maximum and minimum values are amplified by an opposing current, whereas a following current attenuates them.

The mean, maximum, and standard deviation of the surge, heave, and pitch motion responses are provided in Table 5. It can be seen that an opposing current increases the mean values of the three motion responses while a following current decreases them. In the absence of wind, the opposing current can increase the maximum surge and heave responses by up to 40% when interacting with regular waves (i.e. LC2 and LC4). On the other hand, when interacting with irregular waves (i.e. LC6 and LC8), the opposing current can increase surge motion by up to 26% and heave motion by up to 30%, while the following current decreases both surge and heave motions (i.e. LC1, LC3, LC5 and LC7). The interaction has minimally affected the pitch motion, even though this can induce an extra restoring force in the negative heave direction. Accordingly, the heave response has experienced alterations when considering the nonlinear coupling effect of heave and pitch responses, particularly for a single-point mooring system (Li et al., 2018; Qu et al., 2020).

The inclusion of wind speed in operational load cases induced stronger responses of surge, heave, and pitch in operational sea states compared to extreme sea states, as highlighted in Table 5. This observation is attributed to the significant impact of wind on FOWTs, even when parked under extreme sea conditions. The aerodynamics of wind are expected to be the dominant loading in extreme wind events, potentially diminishing the comparative impact of WCI on the floating system. The deliberate exclusion of wind in extreme sea states aligns with the rationale of highlighting the impact of WCI during conditions where it might be more pronounced. Nevertheless, it is imperative to acknowledge the significant impact of wind on the twin-turbine system and the importance of including it in the operational conditions. Thus, these load cases (LC9–LC12) were selected to mirror the environmental conditions of the reference site, providing additional insights into the system's behaviour under realistic scenarios (Chen and Basu, 2018). These findings underline the significance of simulating holistic environmental conditions, encompassing both wind and WCI dynamics, to comprehensively estimate the dynamics of FOWTs. Hence, it is crucial to understand the intricate interaction between wind and wave–current dynamics and their combined implications.

5.3. Effect of wave–current interaction on mooring dynamics

The effect of WCI on mooring dynamics is studied by analysing the effective tension at each line's fairlead. Figs. 8 and 9 show the statistical results of the mooring tension's time series. The configuration of the three mooring lines is depicted in Fig. 3.b, with mooring line A aligned along the positive X-axis. Given the mooring system's symmetry with respect to the X-axis, the responses of mooring lines B and C are identical. The emphasis is, therefore, on presenting the outcomes of lines A and B. In order to provide a clearer illustration of the effect of WCI, the results are presented separately for extreme load cases (LC1–LC8) and operational load cases (LC9–LC12) under favourable and adverse current scenarios. WCI was found to impact the mooring lines' mean and

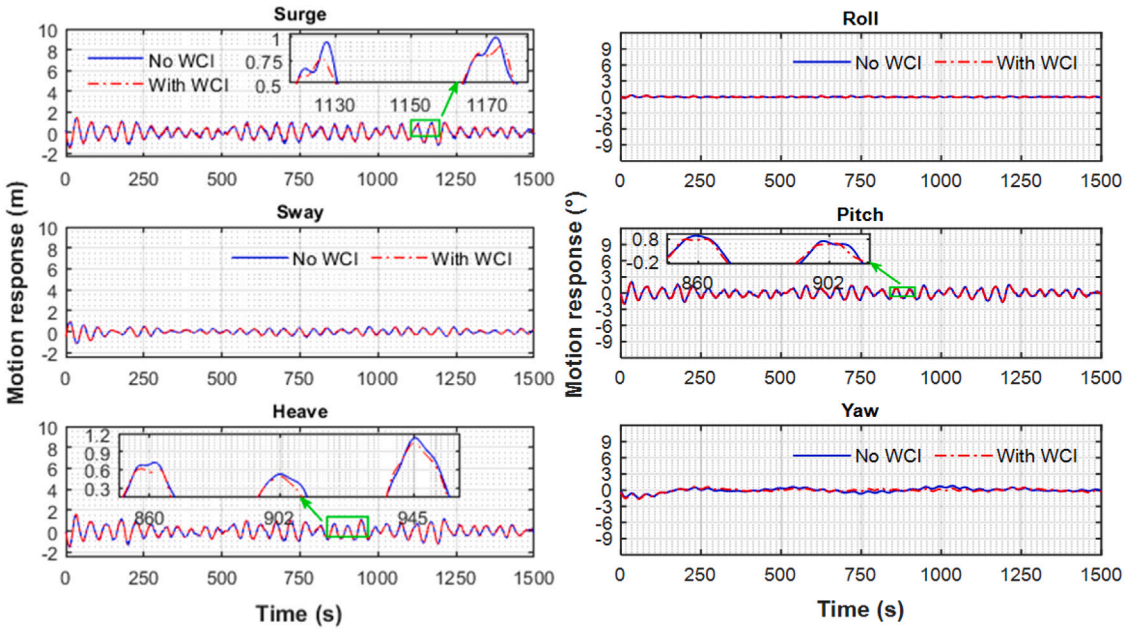

Fig. 6. Time histories of the FOWT motion responses considering wave–current interaction for the operation load case of a favourable current, LC11: (left) translational; (right) rotational.

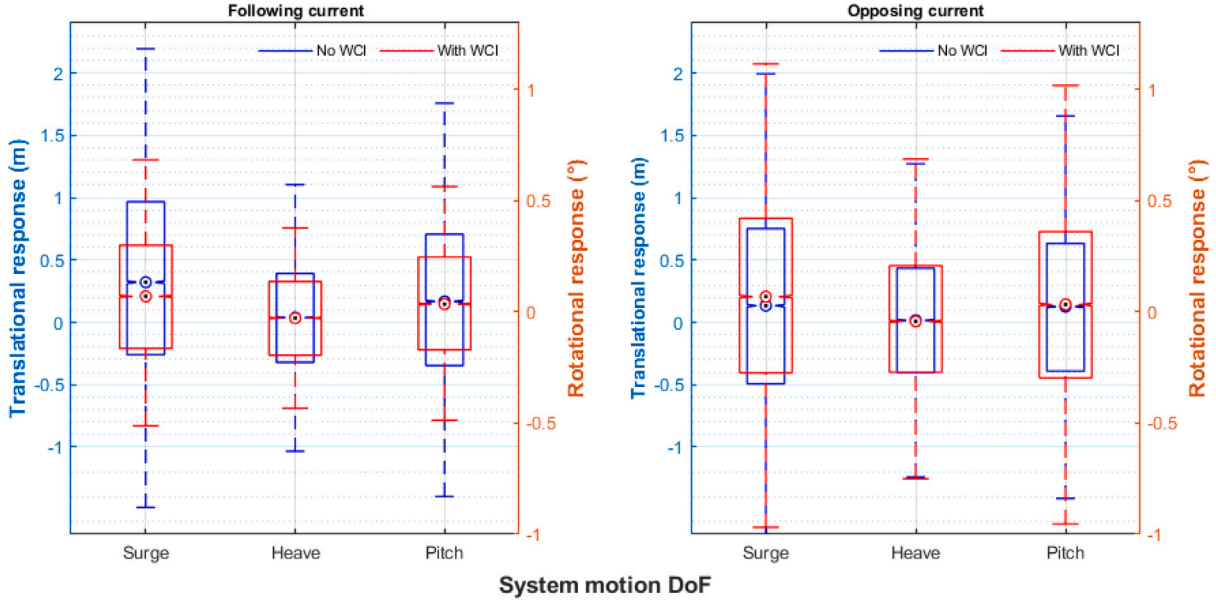

Fig. 7. Statistical distributions of the FOWT motion responses for irregular waves considering wave–current interaction: (left) LC5 with a following current; (right) LC6 with an opposing current.

maximum fairlead tension; in particular, the interaction significantly impacts the maximum tension, while their effect on the mean tension is insignificant, see Figs. 8 and 9. For mooring line A, as depicted in Fig. 8, when regular waves (extreme cases: LC1–LC4) interact with a following current, the maximum tension increases, whereas the opposite effect is observed for an opposing current, with a difference of up to 22%. In the worst-case modelled scenario (LC10), incorporating interaction resulted in a maximum fairlead tension increase of up to 3000 kN, compared to approximately 2450 kN without interaction, indicating a significant 23% increase. The changed surge brought on by WCI may account for these tension load differences. Hence, this highlights the importance of properly handling the increased fairlead tension in mooring design. Therefore, WCI should be included in mooring standards since they partially minimise the uncertainty of the estimated loads, thereby reducing the substantial safety factors that mooring systems are conventionally designed with.

Conversely, line B exhibits the opposite behaviour of the mooring load. Furthermore, despite the negligible effect of interaction on mean line tension for regular waves, an apparent impact was seen in the sea states of the short periods (LC3 and LC4; LC9 and LC10). This can be ascribed to the nonlinearity inherent in the stiffness of the catenary mooring system. Additionally, the dynamics of FOWT in regular seas depend not solely on the effect of current on the wave amplitude but also on the wave frequency due to the resonance effect. On the other hand, differences of up to ±10% have been recorded due to the accounting of such interaction, which is mainly dependent on the arrangement of the mooring cables in relation to the loading conditions. Furthermore, it is important to note that the tension of mooring lines

Table 5
Statistical comparison of FOWT motion responses considering wave–current interaction.

LC	Coupled model	Surge (m)			Heave (m)			Pitch (°)		
No.	With/No WCI	Mean	Max	StdDev	Mean	Max	StdDev	Mean	Max	StdDev
1	No WCI	0.404	2.139	1.231	0.065	1.068	0.910	0.084	0.910	0.583
	With WCI	0.229	3.612	2.347	0.037	3.725	2.520	0.036	0.885	0.591
2	No WCI	0.043	2.978	1.289	0.097	1.312	0.741	0.008	0.963	0.435
	With WCI	0.072	3.606	2.544	0.050	4.792	3.371	0.031	0.512	0.333
3	No WCI	1.529	2.076	0.381	0.069	0.320	0.172	0.096	0.526	0.298
	With WCI	0.155	2.952	1.953	0.024	3.200	2.126	0.023	0.709	0.472
4	No WCI	0.720	1.093	0.435	0.123	0.688	0.240	0.031	0.799	0.180
	With WCI	0.129	5.070	2.174	0.097	4.406	2.815	0.006	0.956	0.400
5	No WCI	0.385	3.481	0.873	0.045	1.743	0.519	0.057	1.540	0.436
	With WCI	0.282	3.937	0.843	0.033	1.811	0.514	0.043	1.589	0.394
6	No WCI	0.136	2.944	0.872	0.017	1.821	0.603	0.025	1.447	0.423
	With WCI	0.212	2.964	0.912	0.025	1.952	0.622	0.037	1.739	0.483
7	No WCI	0.781	3.225	0.600	0.045	0.836	0.196	0.062	1.260	0.306
	With WCI	0.512	2.527	0.493	0.035	0.712	0.186	0.047	1.098	0.293
8	No WCI	0.327	1.146	0.403	0.138	0.985	0.235	0.012	0.825	0.169
	With WCI	0.692	2.225	0.400	0.050	1.128	0.217	0.069	1.291	0.307
9	No WCI	2.587	4.113	0.466	2.488	4.182	0.483	3.223	5.435	0.635
	With WCI	2.581	4.952	1.099	2.496	5.398	1.091	3.240	5.529	0.636
10	No WCI	2.652	4.155	0.417	2.490	4.257	0.473	3.229	5.552	0.622
	With WCI	2.527	5.090	1.087	2.481	5.481	1.257	3.222	5.265	0.635
11	No WCI	2.626	4.168	0.485	2.494	4.219	0.517	3.230	5.528	0.682
	With WCI	2.638	4.192	0.485	2.496	4.253	0.521	3.232	5.512	0.687
12	No WCI	2.627	4.056	0.435	2.491	4.287	0.505	3.230	5.621	0.667
	With WCI	2.628	4.060	0.431	2.491	4.277	0.500	3.231	5.639	0.661

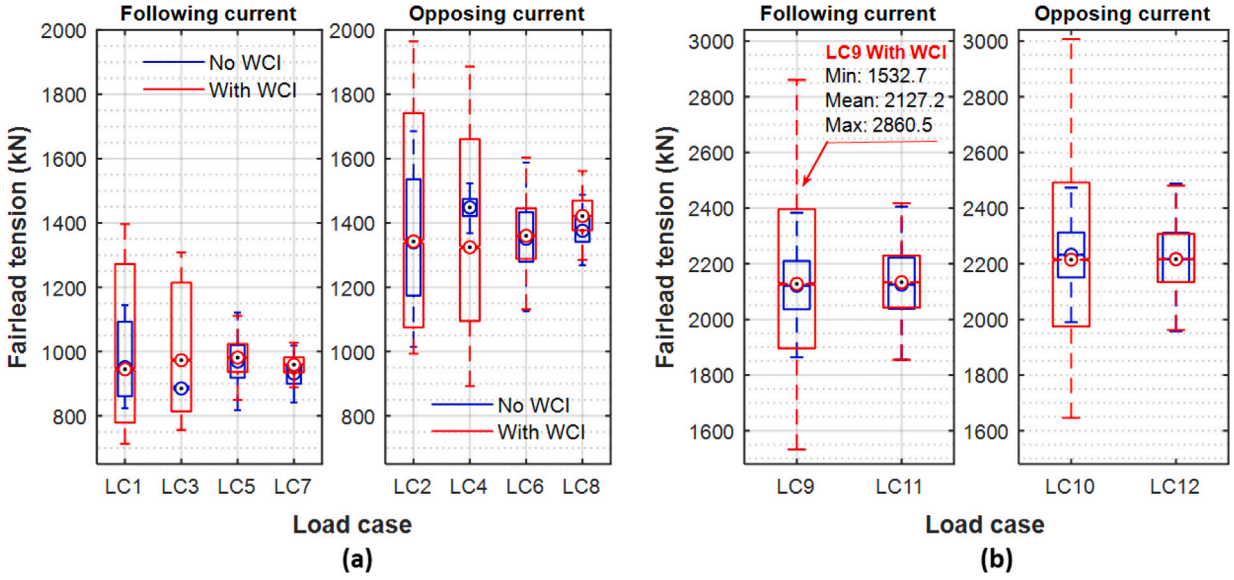

Fig. 8. Effect of wave–current interaction on the mooring tension of line A for different load cases: (a) extreme; (b) operational.

is intricately connected to the surge motion, which is prominently influenced by the presence of the current (Pillai et al., 2018).

5.4. Effect of wave–current interaction on nacelles dynamics

Ensuring the nacelle accelerations of a FOWT system remain within acceptable limits is crucial for its safe operation in a specific location. Thus, the impact of wave–current interaction on the magnitudes of nacelle accelerations (G) and their longitudinal (surge), transverse (sway), and vertical (heave) components, denoted as G_x, G_y, and G_z, respectively, are analysed for four operational load cases. The findings are presented in Figs. 10 and 11; and Table 6. Fig. 10.a demonstrates that incorporating interaction reduces the maximal longitudinal acceleration, G_x. This reduction is particularly pronounced for regular waves (i.e. LC9 and LC10), where a decrease of up to 48% is observed, whereas irregular waves (LC11, LC12) experienced a drop of up to 22%. Consequently, these reductions notably influence the mean values of acceleration magnitudes, which decrease by approximately 50% and 10% when considering the current interaction with regular and irregular waves, respectively (Fig. 10.b). Since WCI was not relevant for the operational cases and as well as the pitch response was found to be less impacted by such interaction. Thus, the significant changes observed in the G_x could be attributed to the WCI-altered surge.

Furthermore, Table 6 summarises the statistics for nacelles accelerations. Notably, incorporating wave–current interaction reduces the minimum, mean, maximum, and standard deviation values, further emphasising the impact of WCI on the nacelle dynamics. On the contrary, the statistical distribution presented in Fig. 11 reveals minor differences in the transverse (G_y) and vertical (G_z) accelerations when considering the interaction effect. These subtle variations can be attributed to the collinearity of the environmental conditions. It is worth noting that the wind, with a speed of 11.4 m/s, opposes the direction of the waves. Given the dominance of these loads (wind and wave), distinguishing

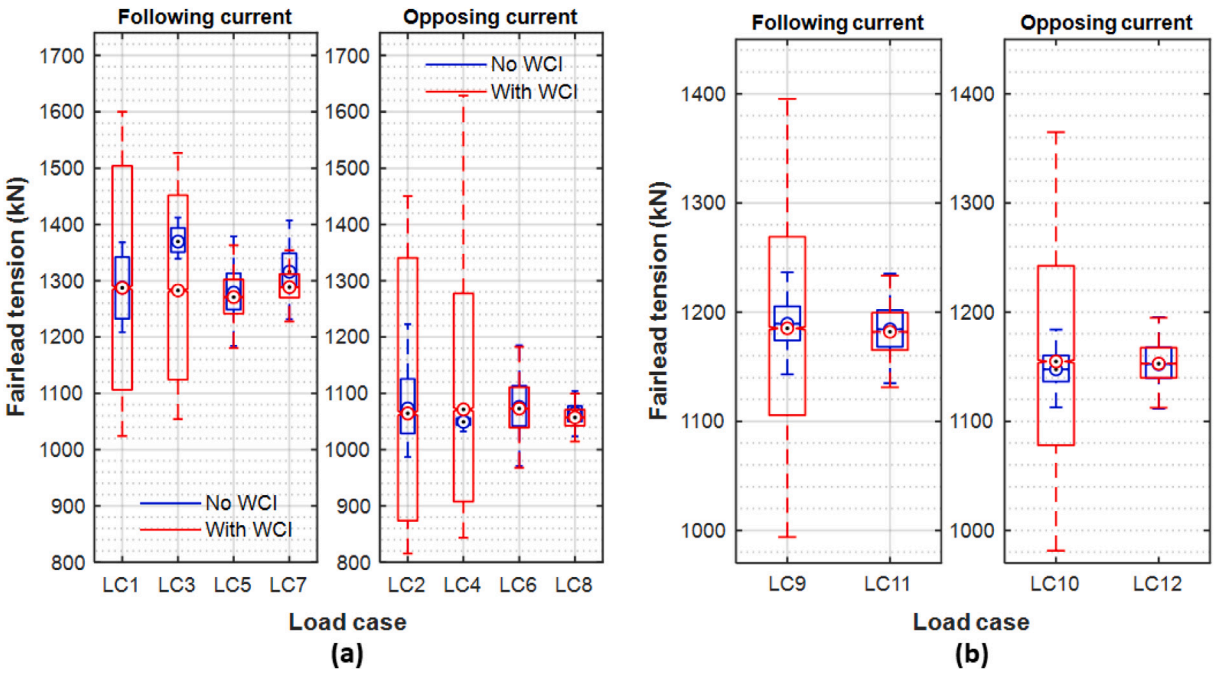

Fig. 9. Effect of wave–current interaction on the mooring tension of line B for different load cases: (a) extreme; (b) operational.

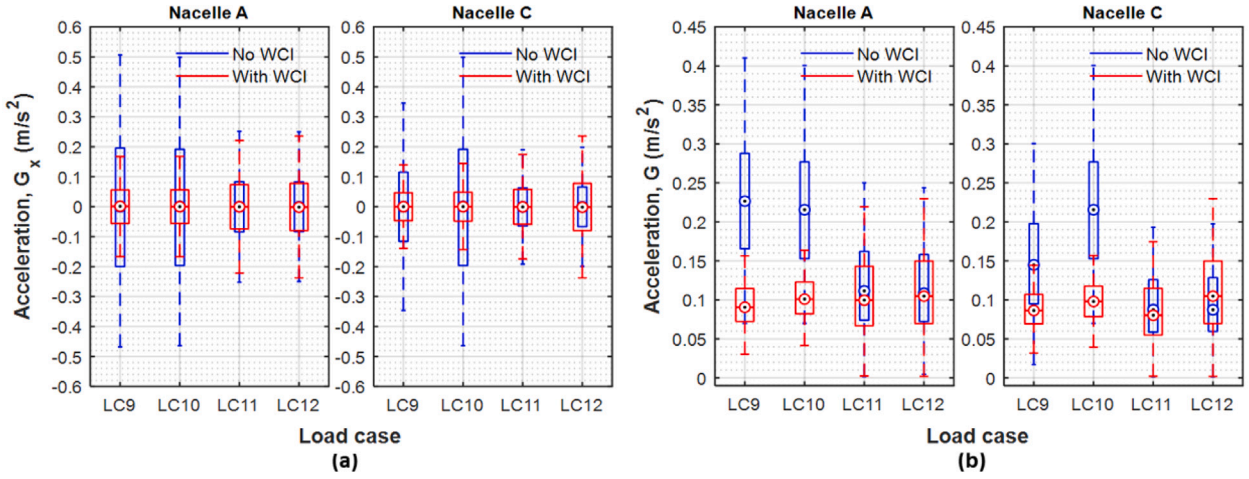

Fig. 10. Effect of wave–current interaction on nacelles accelerations under operational conditions: (a) longitudinal component (G_x); (b) total acceleration (G).

Table 6
Statistical comparison of nacelles' accelerations under operational conditions considering wave–current interaction.

LC	Coupled model	Nacelle A acceleration, G (m^2/s)				Nacelle C acceleration, G (m^2/s)			
No.	With/No WCI	Min	Max	Mean	StdDev	Min	Max	Mean	StdDev
9	No WCI	7.01E−2	5.19E−1	2.30E−1	7.87E−2	1.71E−2	3.97E−1	1.50E−1	6.58E−2
	With WCI	3.84E−3	2.83E−1	9.57E−2	3.47E−2	1.88E−3	2.57E−1	8.96E−2	3.12E−2
10	No WCI	7.01E−2	5.09E−1	2.19E−1	7.84E−2	1.97E−2	4.18E−1	1.62E−1	6.80E−2
	With WCI	4.44E−3	2.64E−1	1.04E−1	3.45E−2	5.65E−3	2.53E−1	9.90E−2	3.23E−2
11	No WCI	1.71E−3	5.14E−1	1.25E−1	6.72E−2	1.45E−3	4.01E−1	9.744E−2	5.23E−2
	With WCI	2.34E−3	3.92E−1	1.11E−1	5.90E−2	2.08E−3	3.26E−1	8.91E−2	4.67E−2
12	No WCI	4.58E−3	4.94E−1	1.21E−1	6.60E−2	1.45E−3	3.97E−1	9.90E−2	5.35E−2
	With WCI	1.89E−3	4.83E−1	1.17E−1	6.33E−2	1.86E−3	4.01E−1	9.63E−2	5.18E−2

the specific influence of the current, with a speed of 0.3 m/s, becomes challenging when it is either following or opposing.

To delve further into the impact of WCI on nacelle structural responses, time series for regular waves and power spectral density (PSD) for irregular waves are depicted in Figs. 12 and 13, respectively. These plots are generated from 0 to 3600 s after excluding the 200-second transient phase during wave build-up. Mean values have been removed for the time series plot, and data has been smoothed to emphasise the dynamics of nacelles' accelerations. As shown in Fig. 12, the consideration of WCI effectively reduces nacelle accelerations. Fig. 13 illustrates the impact of irregular waves, indicating an apparent reduction in acceleration PSDs under the influence of WCI, particularly within the

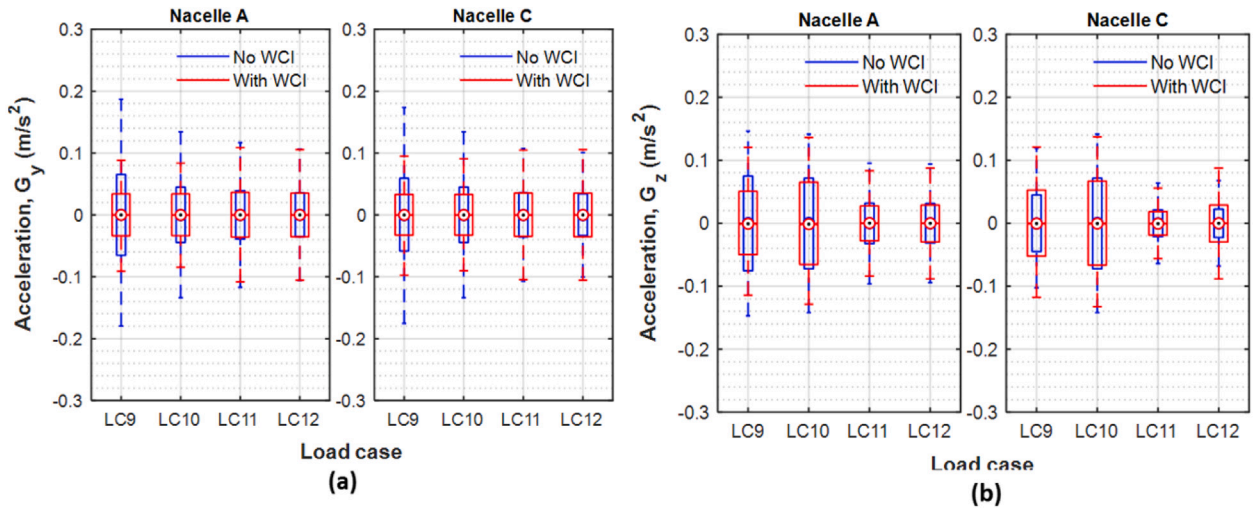

Fig. 11. Effect of wave–current interaction on translational accelerations of the nacelles under operational conditions: (a) transverse component (G_y); (b) vertical component (G_z).

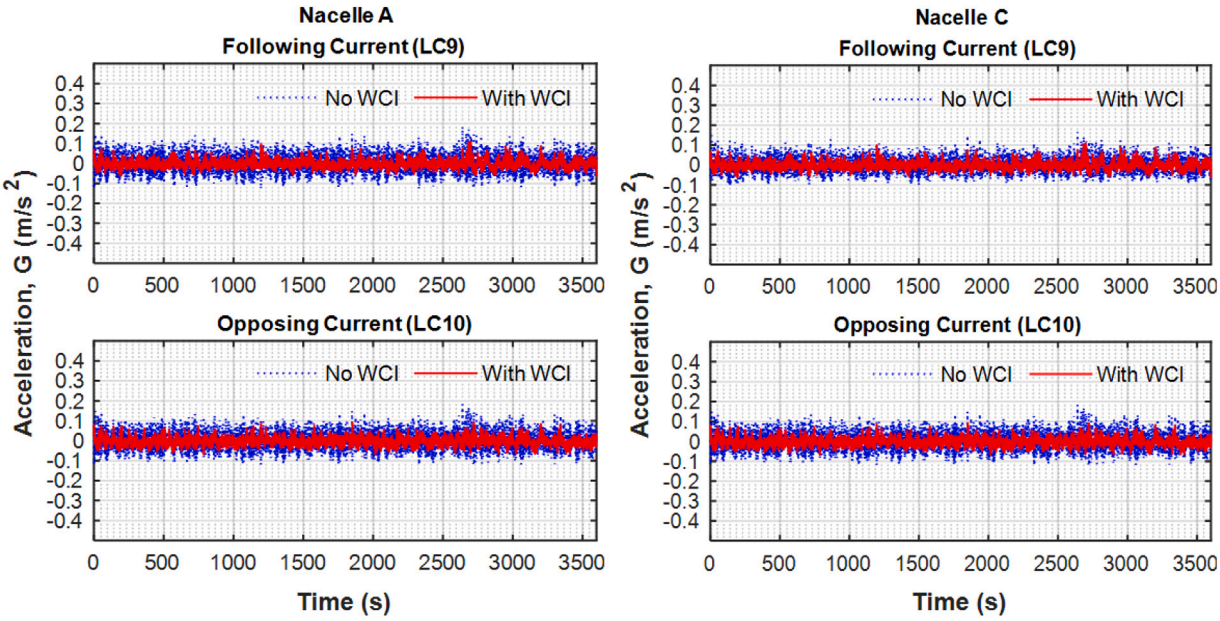

Fig. 12. Time histories of nacelles' accelerations considering wave–current interaction under operational conditions for regular waves: (left) Nacelle A and (right) Nacelle C.

frequency range of 0 to 0.25 Hz, irrespective of the current direction. Interestingly, nacelle A exhibited higher acceleration than nacelle C at very low frequencies.

The observed reductions in nacelles' accelerations when incorporating WCI can be attributed to the complex hydrodynamic interaction caused by the coupling of waves and currents. The intricate WCI introduces additional forces and moments, thereby modifying the flow conditions around the entire floating system. These altered flow fields influence the inertia of the system, which, in turn, contributes to the system's dampening response (Goupee et al., 2014). Furthermore, twin FOWTs add another level of complexity due to the wake interaction between the rotors, which is not considered in this study. Therefore, the assessment of their aerodynamics is a topic of ongoing research (Martín San Román, 2022).

Commonly, the interaction of the current with the incoming waves results in a larger excitation force in surge and excitation moment in pitch. The surge drift force also changes with the current-altered wave height (Chakrabarti, 1984). Unlike conventional offshore structures, FOWTs are distinguished by their towering superstructures. These towers lead to a significant rotor displacement from even a minor pitch motion of the floating platform. Moreover, in this peculiar FOWT design with a single-point mooring system, the presence of wind could potentially tilt the platform, inducing pitch motion and vibrations in the tower fore-aft that could affect nacelle acceleration (Antonutti et al., 2016). Consequently, it impacts the generated power efficiency and contributes to the accumulation of fatigue loads. Therefore, the inclusion of WCI is considerably effective for capturing more accurate wind-wave effects. Then, a trade-off between vibration reduction and rotor speed enhancement could be advantageous for extending the operational life of wind turbine components.

6. Conclusions

This study investigates wave–current interaction effects on the W2Power FOWT, which is equipped with a pair of NREL 5MW wind turbines and moored to the seabed using a single-point mooring system of conventional catenary configuration with three lines made of studless chains. Two analytical models were developed to analyse current interaction with regular and irregular waves. The effects of following and

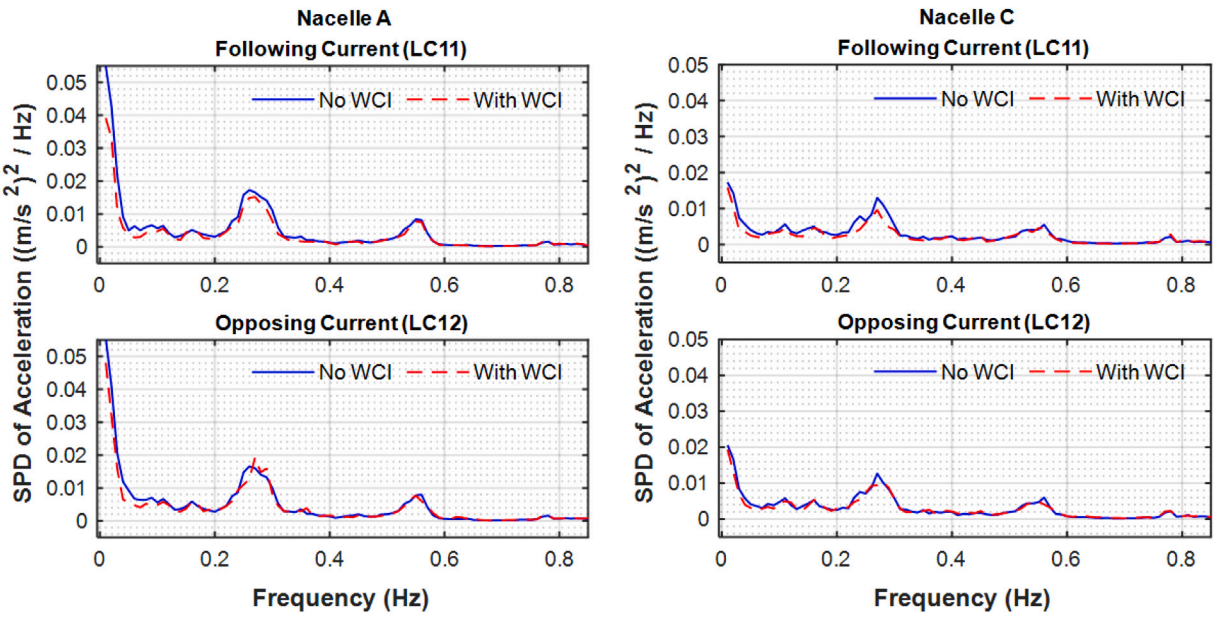

Fig. 13. Power spectral densities of nacelles' accelerations considering wave–current interaction under operational conditions for irregular waves: (left) Nacelle A and (right) Nacelle C.

opposing currents on wave characteristics were investigated, revealing alterations in the regular and stochastic wave fields. WCI models are then integrated with the OrcaFlex programme to analyse the dynamic responses of the floating system. The simulations involved various loading scenarios, including current-only, wave-only, and wave–current with and without interaction. The key findings are as follows:

- The presence of current significantly impacts the FOWT's static equilibrium and, consequently, its mooring system's operational point and motion dynamics.
- WCI significantly affects the translational motion response of the FOWT system, while rotational motion is relatively unaffected. The mean values of surge and heave decreased with a following current and increased with an opposing current, resulting in differences of up to ±26% and ±30%, respectively.
- WCI impacted the mooring system's dynamics, with notable effects observed on the maximum tension at the fairlead, while the mean tension was insignificantly affected. For regular seas, the interaction can lead to differences of up to ±22.5% in the maximum tension, depending on the current direction and mooring layout. For irregular seas, the differences were up to ±10%.
- WCI was found to minimise maximum longitudinal acceleration (G_x) substantially. G_x has experienced a notable decrease of up to 48% in regular seas, while a drop of up to 22% in irregular ones. Transverse and vertical accelerations showed slight variations due to the collinearity of environmental conditions along the X-axis.

The analysis highlights the significance of incorporating WCI to accurately simulate the dynamic responses of FOWTs and ensure operational safety. The current framework and results of the parametric studies presented in this paper can be the basis for the applications of advanced wave–current interaction models in future studies. For instance, nonlinear WCI models, such as those developed by Moreira and Peregrine (2012), can be established to account for more nonlinear effects of such interaction and their implications on the structural responses of FOWTs. Future work will involve the validation of the developed numerical models through tank testing experiments conducted at the Facility (Ingram et al., 2014). This study rigorously examines the FOWT dynamics under extreme sea states and operational conditions, adopting a simplified rigid body approach for the floater subjected to environmental loads. Thus, future research should also consider incorporating floater flexibility in numerical modelling.

CRediT authorship contribution statement

Mujahid Elobeid: Conceptualization, Data curation, Formal analysis, Investigation, Methodology, Software, Validation, Visualization, Writing – original draft, Writing – review & editing. **Ajit C. Pillai:** Conceptualization, Methodology, Writing – review & editing, Project administration, Resources, Supervision. **Longbin Tao:** Conceptualization, Methodology, Project administration, Resources, Supervision, Writing – review & editing. **David Ingram:** Conceptualization, Funding acquisition, Methodology, Project administration, Resources, Supervision, Writing – review & editing. **Jan Erik Hanssen:** Project administration, Resources, Writing – review & editing. **Pedro Mayorga:** Project administration, Resources.

Declaration of competing interest

The authors declare that they have no known competing financial interests or personal relationships that could have appeared to influence the work reported in this paper.

Data availability

The data that has been used is confidential.

References

Antonutti, R., Peyrard, C., Johanning, L., Incecik, A., Ingram, D., 2016. The effects of wind-induced inclination on the dynamics of semi-submersible floating wind turbines in the time domain. Renew. Energy 88, 83–94.

Azcona, J., Palacio, D., Munduate, X., Gonzalez, L., Nygaard, T.A., 2017. Impact of mooring lines dynamics on the fatigue and ultimate loads of three offshore floating wind turbines computed with IEC 61400-3 guideline. Wind Energy 20 (5), 797–813.

Barltrop, N., Varyani, K., Grant, A., Clelland, D., Pham, X., 2007. Investigation into wave—current interactions in marine current turbines. Proc. Inst. Mech. Eng., Part A: J. Power Energy 221 (2), 233–242.

Ben-Israel, A., 1966. A Newton-Raphson method for the solution of systems of equations. J. Math. Anal. Appl. 15 (2), 243–252.

Bretherton, F.P., Garret, C., 1970. Wavetrains in inhomogeneous moving media. Hyperbol. Equ. Waves: Battelle Seattle 1968 Recontres 211–236.

Chakrabarti, S.K., 1984. Steady drift force on vertical cylinder-viscous vs. potential. Appl. Ocean Res. 6 (2), 73–82.

Chen, L., Basu, B., 2018. Fatigue load estimation of a spar-type floating offshore wind turbine considering wave-current interactions. Int. J. Fatigue 116, 421–428.

Chen, L., Basu, B., 2019. Wave-current interaction effects on structural responses of floating offshore wind turbines. Wind Energy 22 (2), 327–339.
Cummins, W., et al., 1962. The Impulse Response Function and Ship Motions. Department of the Navy, David Taylor Model Basin Bethesda, MD, USA.
Dai, J., Abrahamsen, B.C., Viuff, T., Leira, B.J., 2022. Effect of wave-current interaction on a long fjord-crossing floating pontoon bridge. Eng. Struct. 266, 114549.
Davidson, J., Ringwood, J.V., 2017. Mathematical modelling of mooring systems for wave energy converters—A review. Energies 10 (5), 666.
de Jesus Henriques, T., Tedds, S., Botsari, A., Najafian, G., Hedges, T., Sutcliffe, C., Owen, I., Poole, R., 2014. The effects of wave–current interaction on the performance of a model horizontal axis tidal turbine. Int. J. Mar. Energy 8, 17–35.
DNV, 2010. Offshore Standard DNV-OS-E301 Position Mooring. Det Norske Veritas, Høvik, Norway.
DNV, 2019. Environmental Conditions and Environmental Loads. Oslo, Norway, Det Norske Veritas.
Draycott, S., Noble, D., Davey, T., Bruce, T., Ingram, D., Johanning, L., Smith, H., Day, A., Kaklis, P., 2018. Re-creation of site-specific multi-directional waves with non-collinear current. Ocean Eng. 152, 391–403.
Draycott, S., Pillai, A.C., Gabl, R., Davey, T., 2021. Wave buoys in current-experimental results and observations. In: European Wave and Tidal Energy Conference. EWTEC.
Elobeid, M., Tao, L., Ingram, D., Pillai, A.C., Mayorga, P., Hanssen, J.E., 2022. Hydrodynamic performance of an innovative semisubmersible platform with twin wind turbines. In: International Conference on Offshore Mechanics and Arctic Engineering, Vol. 85932. American Society of Mechanical Engineers, V008T09A032.
EnearOcean S.L., 2007. SME marine energy engineering SME, Málaga, Spain. SME Mar. Energy Eng. SME URL https://enerocean.com/.
Facility, F.O.E.R., 2013. FloWave Ocean Energy Research Facility. The University of Edinburgh, Edinburgh, UK, URL www.flowavett.co.uk.
Faltinsen, O., 1993. Sea Loads on Ships and Offshore Structures, Vol. 1. Cambridge University Press.
Fenton, J.D., McKee, W., 1990. On calculating the lengths of water waves. Coast. Eng. 14 (6), 499–513.
Froude, W., 1920. On the Elementary Relation Between Pitch, Slip, and Propulsive Efficiency. Technical Report.
GeinE, 2020. SESAM-GeniE Manual. Det Norske Veritas (DNV), Oslo, Norway, URL www.dnv.com.
Gonçalves, R.T., Chame, M.E., Silva, L.S., Koop, A., Hirabayashi, S., Suzuki, H., 2021. Experimental flow-induced motions of a FOWT semi-submersible type (OC4 phase II floater). J. Offshore Mech. Arct. Eng. 143 (1).
Goupee, A.J., Koo, B.J., Kimball, R.W., Lambrakos, K.F., Dagher, H.J., 2014. Experimental comparison of three floating wind turbine concepts. J. Offshore Mech. Arct. Eng. 136 (2), 020906.
Hall, M., Buckham, B., Crawford, C., 2014. Evaluating the importance of mooring line model fidelity in floating offshore wind turbine simulations. Wind Energy 17 (12), 1835–1853.
Hanssen, J.E., Margheritini, L., Mayorga, P., Hezari, R., O'Sullivan, K., Martinez, I., Arriaga, A., Agos, I., Todalshaug, J.H., Steynor, J., Ingram, D., 2015. Design and performance validation of a hybrid offshore renewable energy platform: A path to cost-efficient development of deepwater marine energy resources. In: The 10th International Conference on Ecological Vehicles and Renewable Energies, EVER 2015.
Hasselmann, K., Barnett, T.P., Bouws, E., Carlson, H., Cartwright, D.E., Enke, K., Ewing, J., Gienapp, A., Hasselmann, D., Kruseman, P., et al., 1973. Measurements of wind-wave growth and swell decay during the joint north sea wave project (JONSWAP). Ergaenzungsheft Deutschen Hydrographischen Z., Reihe A.
Hedges, T., 1981. Some effects of currents on wave spectra. In: Proceedings of the First Indian Conference in Ocean Engineering, Vol. 1. pp. 30–35.
Hedges, T.S., Anastasiou, K., Gabriel, D., 1985. Interaction of random waves and currents. J. Waterw., Port, Coastal, Ocean Eng. 111 (2), 275–288.
Huang, N.E., Chen, D.T., Tung, C.C., Smith, J.R., 1972. Interactions between steady won-uniform currents and gravity waves with applications for current measurements. J. Phys. Oceanogr. 2 (4), 420–431.
Ingram, D., Wallace, R., Robinson, A., Bryden, I., 2014. The design and commissioning of the first, circular, combined current and wave test basin. In: Proceedings of the Oceans.
Isaacson, M., Cheung, K.F., 1993. Time-domain solution for wave—current interactions with a two-dimensional body. Appl. Ocean Res. 15 (1), 39–52.
Ismail, N.M., 1984. Wave-current models for design of marine structures. J. Waterw., Port, Coastal, Ocean Eng. 110 (4), 432–447.
Jonkman, J.M., 2007. Dynamics Modeling and Loads Analysis of an Offshore Floating Wind Turbine. University of Colorado at Boulder.
Jonkman, J., 2010. Definition of the Floating System for Phase IV of OC3. Technical Report, National Renewable Energy Lab.(NREL), Golden, CO (United States).
Jonkman, J., Butterfield, S., Musial, W., Scott, G., 2009. Definition of a 5-MW Reference Wind Turbine for Offshore System Development. Technical Report, National Renewable Energy Lab.(NREL), Golden, CO (United States).
Jonkman, B., Kilcher, L., 2012. TurbSim User's Guide: Version 1.06. 00. National Renewable Energy Laboratory, Golden, CO, USA.
Jonsson, I.G., 1990. Wave-current interactions. Sea, A 9, 65–120.
Lai, R.J., Long, S.R., Huang, N.E., 1989. Laboratory studies of wave-current interaction: Kinematics of the strong interaction. J. Geophys. Res.: Oceans 94 (C11), 16201–16214.
Li, Y., Liu, L., Zhu, Q., Guo, Y., Hu, Z., Tang, Y., 2018. Influence of vortex-induced loads on the motion of SPAR-type wind turbine: A coupled aero-hydro-vortex-mooring investigation. J. Offshore Mech. Arct. Eng. 140 (5).
Martín San Román, R., 2022. Coupled Dynamics of Multi Wind Turbine Floating Platforms (Ph.D. thesis). Espacio.
Masson, D., 1996. A case study of wave–current interaction in a strong tidal current. J. Phys. Oceanogr. 26 (3), 359–372.
Moreira, R., Peregrine, D., 2012. Nonlinear interactions between deep-water waves and currents. J. Fluid Mech. 691, 1–25.
Morison, J., Johnson, J.W., Schaaf, S.A., 1950. The force exerted by surface waves on piles. J. Pet. Technol. 2 (05), 149–154.
Nestegård, A., Ronæss, M., Hagen, Ø., Ronold, K., Bitner-Gregersen, E.M., 2019. Recommended Practice DNV-RP-C205: On Environmental Conditions and Environmental Loads. Det Norske Veritas (DNV), Oslo, Norway.
Nguyen, H.X., 2022. Dynamic Response of Spar-Type Floating Offshore Wind (Ph.D. thesis). Trinity College Dublin. School of Engineering. Disc of Civil Structural ....
NKUA-AM&WFG, 2021. Long-term Hincast Data from: Atmospheric Modeling and Weather Forecasting Group (AM&WFG). National & Kapodistrian University of Athens, Athens, Greece, URL https://forecast.uoa.gr/en/group.
OrcaFlex, 2023. Orcaflex Manual. Orcina Ltd, Cumbria, UK, URL www.orcina.com.
OrcaWave, 2023. OrcaWave Manual. Orcina Ltd, Cumbria, UK, URL www.orcina.com.
Palm, J., Eskilsson, C., Paredes, G.M., Bergdahl, L., 2016. Coupled mooring analysis for floating wave energy converters using CFD: Formulation and validation. Int. J. Mar. Energy 16, 83–99.
Peeringa, J.M., 2014. Fatigue loading on a 5MW offshore wind turbine due to the combined action of waves and current. J. Phys.: Conf. Ser. 524 (1), 012093.
Peters, H., Boonstra, H., 1988. Fatigue loading on a single pile platform due to combined action of waves and currents.
Phillips, .M., 1977. The dynamics of the upper ocean. J. Fluid Mech. 88 (4), 793–794.
Pierson, Jr., W.J., Moskowitz, L., 1964. A proposed spectral form for fully developed wind seas based on the similarity theory of SA kitaigorodskii. J. Geophys. Res. 69 (24), 5181–5190.
Pillai, A.C., Davey, T., Draycott, S., 2021. A framework for processing wave buoy measurements in the presence of current. Appl. Ocean Res. 106, 102420.
Pillai, A.C., Thies, P.R., Johanning, L., 2018. Optimization of mooring line axial stiffness characteristics for offshore renewable energy applications. In: ISOPE International Ocean and Polar Engineering Conference. ISOPE, ISOPE–I.
Qu, X., Li, Y., Tang, Y., Hu, Z., Zhang, P., Yin, T., 2020. Dynamic response of spar-type floating offshore wind turbine in freak wave considering the wave-current interaction effect. Appl. Ocean Res. 100, 102178.
Rognebakke, O., 2002. Sloshing in Rectangular Tanks and Interaction with Ship Motions. Fakultet for ingeniørvitenskap og teknologi.
Sarkar, S., Chen, L., Fitzgerald, B., Basu, B., 2020. Multi-resolution wavelet pitch controller for spar-type floating offshore wind turbines including wave-current interactions. J. Sound Vib. 470, 115170.
Shin, H., 2011. Model test of the OC3-hywind floating offshore wind turbine. In: The Twenty-First International Offshore and Polar Engineering Conference. OnePetro.
Silva, L., Cazzolato, B., Sergiienko, N., Ding, B., 2021. Nonlinear dynamics of a floating offshore wind turbine platform via statistical quadratization—Mooring, wave and current interaction. Ocean Eng. 236, 109471.
Silva, M., Vitola, M., Esperança, P., Sphaier, S., Levi, C., 2016. Numerical simulations of wave–current flow in an ocean basin. Appl. Ocean Res. 61, 32–41.
Smith, J.M., 1997. One-Dimensional Wave-Current Interaction. Technical Report, Engineer Research and Development Center Vicksburg Ms Coastal and Hydraulics Lab.
Soares, C.G., De Pablo, H., 2006. Experimental study of the transformation of wave spectra by a uniform current. Ocean Eng. 33 (3–4), 293–310.
Solidworks, 2021. Solidworks Manual. Dassault Systèmes SOLIDWORKS Corp, Waltham, Massachusetts, USA, URL www.solidworks.com.
Thomas, G., 1981. Wave-current interactions: an experimental and numerical study. Part 1. linear waves. J. Fluid Mech. 110, 457–474.
Tung, C.C., Huang, N.E., 1974. Influence of current on statistical properties of waves. J. Waterw., Harbors Coastal Eng. Div. 100 (4), 267–278.
Van den Boom, H., 1985. Dynamic behaviour of mooring lines. In: BOSS Conference, Vol. 1. pp. 359–368.
White, B.S., 1999. Wave action on currents with vorticity. J. Fluid Mech. 386, 329–344.
WindEurope, 2018. Floating offshore wind energy: A policy blueprint for europe. pp. 2–3, URL www.windeurope.org.
Zhao, R., Faltinsen, O.M., Krokstad, J., Aanesland, V., 1988. Wave-current interaction effects on large-volume structures. In: BOSS'88. pp. 623–638.